ChemCatChem

Research Article
doi.org/10.1002/cctc.202500396

Chemistry Europe
European Chemical Societies Publishing

www.chemcatchem.org

Sol–Gel Synthesized Co-Doped Ilmenite-$NiTiO_3$ for Oxygen Evolution Reaction: Interplay of Inductive Effect and Crystal Structure

Shraddha Jaiswal,[a] Subash Chandra Gupta,[a] and Asha Gupta*[a]

The oxygen evolution reaction is key to advancing hydrogen production, energy storage, and sustainable energy technologies. In this study, we have explored the ilmenite-type Co-substituted $NiTiO_3$ as a promising OER catalyst in the alkaline electrolyte. Synergistic interaction between Ni and Co generates the inductive effect which enhances the ionicity of Ni—O bond leading to a greater overlap between Ni(3*d*) and O(2*p*) orbitals, resulting in a higher OER activity of the doped catalysts. Further presence of surface active Co^{3+} in the ilmenite structure plays a key role in the enhancement of OER activity of the catalyst. A systematic investigation of the OER activity of $Ni_{1-x}Co_xTiO_3$ ($0 < x < 0.25$) with different amounts of Co doping synthesized via sol–gel method is reported here. Among the compositions investigated, $Ni_{0.825}Co_{0.175}TiO_3$ is the most active as it exhibits excellent activity with a Tafel slope of 56 mV dec^{-1} and a overpotential of 395 mV at 10 mA cm^{-2}. This work presents the role of the inductive effect originating due to the difference in the electronegativity of neighboring cations, leading to alteration of the redox energies and facilitating the effective electron transfer required for the electrocatalytic OER, which can be further utilized to develop superior electrocatalysts.

1. . Introduction

The excessive utilization of carbon-based fossil fuels has shown a detrimental effect on the environment. Therefore, the researchers are driven to discover alternative, environment-friendly and sustainable energy systems to fulfill the need for energy.[1] Several innovative ideas and strategies have been created to achieve efficient and environment-friendly alternative/renewable energy conversion and storage systems, such as supercapacitors, batteries, photocatalysis, and electrocatalysis.[2–5] Water electrolysis is a green and clean approach for the production of H_2 and O_2. Overall electrochemical water splitting is a promising energy conversion method that incorporates two half-reactions: the hydrogen evolution reaction (HER) at the cathode and the oxygen evolution reaction (OER) at the anode. However, OER is slower than HER because it is four electrons transfer reaction, whereas HER involves two electrons transfer. Thus, the OER is crucial for the overall effectiveness of electrocatalytic water splitting.[6]

$$2H_2O \rightarrow O_2 + 4H^+ + 4e^- \quad (1)$$

The OER and oxygen reduction reaction (ORR) are crucial electrochemical processes that significantly impact the efficiency of fuel cells and metal-air batteries.[7] Although some noble metals and their corresponding compounds, such as Pt, RuO**2**, and IrO**2**, demonstrate significant catalytic activity for ORR or OER, their extensive utilization or large-scale use is hindered by their high cost and limited availability.[8,9]

Many efforts have been made to substitute benchmark catalysts with transition metal-based materials for the OER. Among these alternatives, nickel-based catalysts have shown promising catalytic activity for OER in alkaline environments.[10] The strategic design of nickel oxide-based materials provides a reliable approach to utilize the synergistic interactions among the constituent materials, aiding in addressing the challenges associated with oxygen electrocatalysis.[11] Consequently, a wide variety of transition-metal compounds, including transition-metal oxides (e.g., Mn, Fe, Co, and Ni), (oxy)hydroxides, chalcogenides, carbides, phosphides, nitrides, and their related composite electrocatalysts, have been synthesized.[12] The advancement of oxygen evolution catalysts (OECs) for electrocatalytic methods, which has seemingly received more attention, has resulted in the emergence of several widely recognized Co- and Ni-based materials.[13] Most investigations into the OER primarily focus on perovskite and spinel-type oxides, however, there has been limited exploration of other nickel-based mixed metal oxides, specifically ABO_3-type ilmenites.[14]

The synthesized $NiTiO_3$ exhibits an ilmenite-type structure characterized by octahedral coordination of both nickel and titanium cations. In this arrangement, the cation layers are alternately occupied by Ni^{2+} and Ti^{4+} ions, while both the corundum and ilmenite structures display six-fold coordination with oxygen. The coordination number and arrangement of cations in $NiTiO_3$ play a significant role in shaping their electronic, magnetic, and catalytic properties, which in turn influence their potential applications in advanced technologies.[15]

[a] *S. Jaiswal, S. Chandra Gupta, A. Gupta*
Department of Chemistry, Indian Institute of Technology (Banaras Hindu University), Varanasi, Uttar Pradesh 221005, India
E-mail: asha.chy@itbhu.ac.in

Supporting information for this article is available on the WWW under https://doi.org/10.1002/cctc.202500396

In line with this methodology, several types of ABO_3 perovskites have been evaluated for their electrocatalytic activity in the oxygen evolution reaction.[16,17] Various formations, including earth-abundant elements in the transition metal position (B), such as $LaNiO_3$ and $LaCoO_3$, exhibited an activity trend outlined as Ni > Co > Fe > Mn > Cr. These results emphasized the exceptional catalytic efficiency of Ni and Co, which has also been demonstrated in recent investigations, including various materials with structures resembling $BaNiO_3$, like $Ba_{0.5}Sr_{0.5}Co_{0.8}Fe_{0.2}O_3$.[17] Some researchers have found that the combination of Ni and Co into $Ni_xCo_{3-x}O_4$[18–20] systems exhibits enhanced activity for the oxygen evolution reaction. Similarly, many nickel and cobalt incorporated hetero-structures, such as ultrafine NiO nanosheets supported by TiO_2,[21] cobalt-doped black TiO_2 nanotube arrays,[22] polymorph-$NiTiO_3$,[23] and $NiTiO_3$/Ni[24] are of particular relevance for OER in basic media.

Following this strategy and motivated by the high performances of Ni and Co-based materials as OER catalysts, we present the successful synthesis of Co-doped $NiTiO_3$ ilmenite structure via the sol–gel method and evaluate it as an electrocatalyst for OER. Ni, Ti, and Co have their distinct oxidation states (4 + for Ti, 2 + for Ni, and 2+/3 + for Co) in the ilmenite structure. The incorporation of foreign metal substituents to adjust the redox potential has been demonstrated as a very efficient approach to enhance the efficiency of oxygen electrocatalysis.[25] The inductive effect, resulting from differences in electronegativity, is commonly observed in multi-component materials. More electronegative substitutes or components tend to draw the electron cloud of chemical bonds, which provides the tuned surface electronic structure of the catalyst.[26]

The presence of Co^{3+} at the Ni site within the ilmenite lattice $Ni_{1-x}Co_xTiO_3$ induces an inductive effect that enhances the OER activity. From linear sweep voltammograms (LSV) results, we found that cobalt doping in $Ni_{1-x}Co_xTiO_3$ ($0 \leq x \leq 0.25$) increases the OER activity, and the best OER activity is achieved for $Ni_{0.825}Co_{0.175}TiO_3$ with a Tafel slope of 56 mV dec^{-1} and an overpotential of 395 mV at a current density of 10 mA cm^{-2}.

2. Experimental Section

2.1. Material Synthesis

A sol–gel synthesis route was utilized to synthesize polycrystalline $Ni_{1-x}Co_xTiO_3$ (x = 0, 0.05, 0.1, 0.15, 0.175, 0.2, 0.25) powder sample. Stoichiometric quantity of precursor compounds such as $Ni(CH_3COO)_2.6H_2O$ (Sigma-Aldrich, ≥99%), $Co(CH_3COO)_2.6H_2O$ (Sigma-Aldrich, ≥99%) $(C_3H_7O)_4Ti$, titanium isopropoxide (TIP) (Sigma-Aldrich, ≥98%), were used as received without further purification. Double-distilled water was used during all of the experimental processes. A stoichiometric amount of $Ni(CH_3COO)_2.4H_2O$ and $Co(CH_3COO)_2.4H_2O$ was dissolved in 35 mL of ethylene glycol solution, referred to as solution A. The mixture was stirred for half an hour at 80 °C on a hot plate. In 5 mL of cold dilute HNO_3, the stoichiometrically calculated amount of TIP was added and stirred to get a clear solution followed by adding it to the above solution A. Then the reaction was continued for 6 h with stirring at 80 °C. The sample mixture was initially heated at 400 °C for 1 h. Finally, different colors of undoped and doped $NiTiO_3$ samples were obtained by heating the samples in a sintering muffle furnace at 800 °C for 3 h with an intermediate grinding step to get single-phase material with a heating rate of 5 °C/min in air. The series of $Ni_{1-x}Co_xTiO_3$ samples were denoted as NCTO-0, NCTO-5, NCTO-10, NCTO-15, NCTO-17.5, NCTO-20, and NCTO-25 for (x = 0.05, 0.1, 0.15, 0.175, 0.2, 0.25), respectively, in this manuscript.

2.2. Physical Characterization

The phase identification and crystallinity of synthesized samples were confirmed by powder X-ray diffraction method by employing Rigaku Miniflex X-ray diffractometer with Cu Kα radiation (λ = 1.54 Å), with a scan rate of 3° min^{-1} in the 2θ range of 20°–90°. The structure was refined by the Rietveld refinement method using FULLPROF suite software. Fourier-transform infrared (FT-IR) spectra were recorded using a Perkin Elmer FT-IR spectrometer, and the specimens were pressed into small thin pellets made with pure KBr and the sample. X-ray photoelectron spectroscopy (XPS) studies were carried out using a Thermo Scientific Multilab 2000 instrument with Al Kα radiation operated at 150 W to investigate the electronic structures of the materials. All the binding energy values were charge-corrected to adventitious C 1s at 284.5 eV, and the peak deconvolution was carried out with the help of XPSPEAK41 software. The morphology and microstructure of the calcined materials were analyzed using a high-resolution scanning electron microscope (HR-SEM) (using Nova Nano SEM 450), and the elemental compositions of the materials were analyzed by the energy-dispersive X-ray (EDX) analysis method with a probe attached to the HR-SEM instrument. The lattice spacing was measured by taking an HR-TEM image (FEI TECNAI G2 20 TWIN) of the sample operated at 300 kV.

2.3. Sample Preparation for Electrochemical Measurements

The electrochemical studies were conducted using an electrochemical workstation, specifically a Pine research instrument (Wave driver 200). A three-electrode system was employed, that included a working electrode made of catalyst-coated carbon paper with an area of 1 cm^2, an Ag/AgCl/4 M KCl reference electrode, and a platinum wire as the counter electrode. The homogeneous catalyst ink was prepared by sonicating a mixture of 20 mg of the catalyst sample, 5 mg of activated carbon, and 5 µL of Nafion binder in 1 mL of *N*-methyl pyrrolidone (NMP) for a duration of 30 min. The ink was carefully drop-casted onto carbon paper and subsequently dried in a vacuum oven at 80 °C for a duration of 12 h. The optimal mass loading of the active material on the substrate was kept 1 mg cm^{-2}.[27] The electrochemical analysis was conducted using Aftermath software, employing techniques such as cyclic voltammetry (CV), linear sweep voltammetry (LSV), chronoamperometric (CA), and electrochemical impedance spectroscopy (EIS) in an O_2-saturated 1 M KOH electrolyte. Prior to conducting each set of experiments, the electrolyte solutions were freshly prepared utilizing analytical grade KOH and deionized water. All potentials are reported versus the reversible hydrogen electrode (RHE) in this manuscript, and for the conversion of the obtained potential (versus Ag/AgCl) to RHE, the following equation was used:

$$E_{RHE} = E_{Ag/AgCl} + 0.059\ pH + E^0_{Ag/AgCl} \quad (2)$$

where, $E^0_{Ag/AgCl}$ (in 4 M KCl) = + 0.199 V; pH = 13.8 for 1 M KOH.

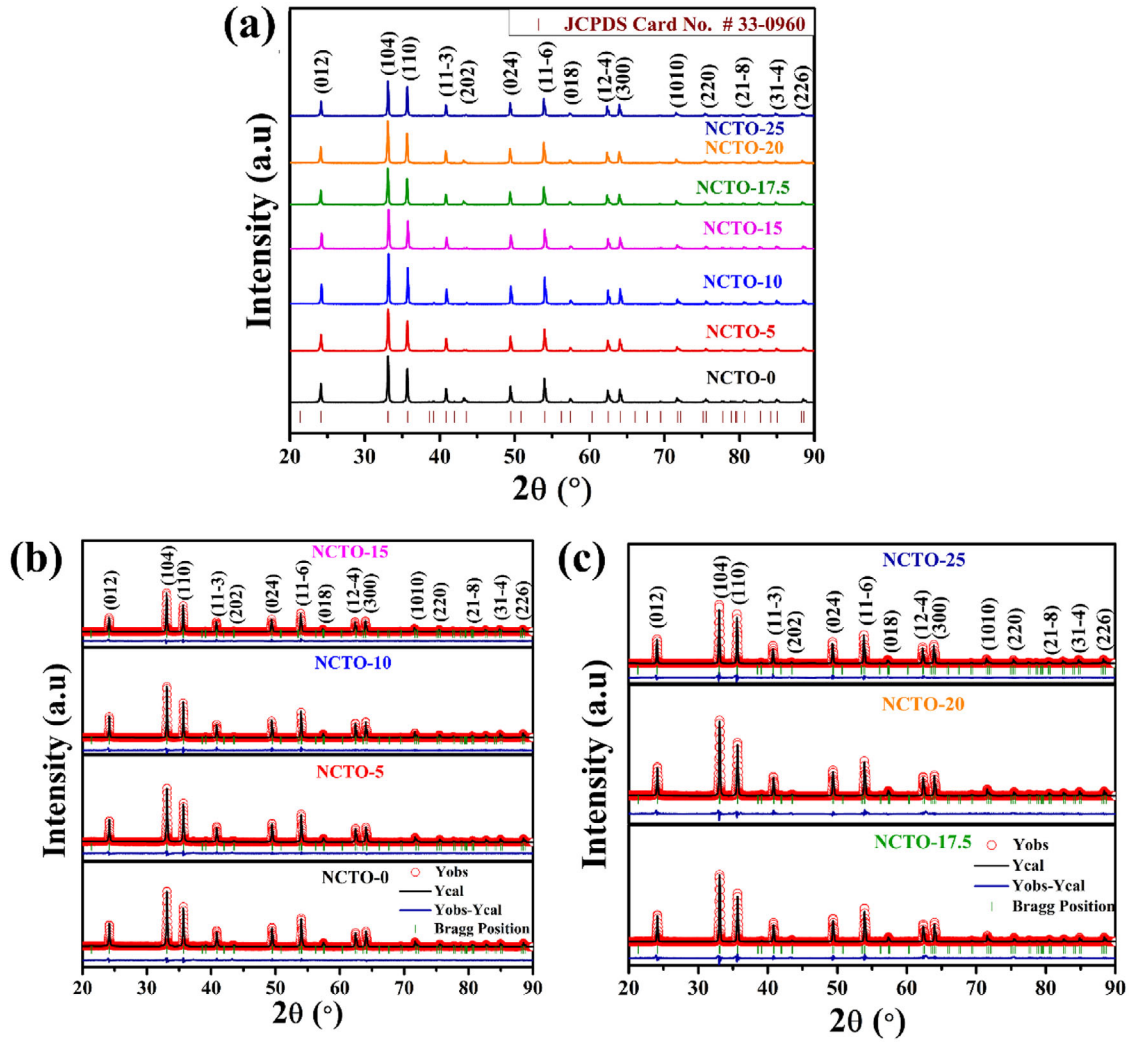

Figure 1. (a) XRD pattern of sol–gel synthesized NCTO samples. (b,c) Rietveld refined XRD profile of $Ni_{1-x}Co_xTiO_3$ (x = 0.05, 0.1, 0.15, 0.175, 0.2, 0.25).

3. Results and Discussion

3.1. XRD Studies Rietveld Refinement

The well-separated diffraction peaks of the $Ni_{1-x}Co_xTiO_3$ (x = 0.05, 0.1, 0.15, 0.175, 0.2, 0.25) samples in the XRD pattern in Figure 1a confirm the presence of ilmenite $NiTiO_3$ with a rhombohedral phase *R-3* (148) space group. These peaks are indicative of the material's crystalline form and are well-indexed with the $NiTiO_3$ (JCPDS No. 33–0960). The X-ray diffraction spectrum is also utilized to estimate the average crystallite size D of $Ni_{1-x}Co_xTiO_3$ (x = 0–0.25) samples using the Debye–Scherrer formula as follows:

$$D = 0.9\lambda/\beta cos\Theta \quad (3)$$

where λ is the wavelength of the X-ray radiation (1.54 Å for Cu Kα), β is the full-width half maxima and θ is the diffraction angle.[28] The average crystallite size was found to increase from ˜41.1 (±1) to ˜49.3 (±1) nm with increasing doping percentage of Co. This is due to the larger ionic radii of the dopant ion Co^{2+} (0.72 Å) compared to Ni^{2+} ions (0.69 Å). Further, Rietveld refinement of NCTO samples was performed by taking Pseudo-Voigt as peak profile function, rhombohedral phase, and R-3 (148) space group, shown in Figure 1b,c. The refinement results, along with their reliability factors (R_{wp} and χ^2), were listed in Table 1. It is clear from the refinement that the lattice parameter slightly increases in comparison with the pure $NiTiO_3$ because of the larger ionic radius of Co^{2+} than Ni^{2+}. To evaluate how the introduction of Co influences the stability of the crystal structure, the Goldschmidt tolerance (t) factor defined for an ABO_3–type ilmenite structure was evaluated as follows:[29,30]

$$t = \frac{1}{3}\left(\frac{\left(\sqrt{2}+1\right)R_O^{-2}+R_B)}{R_O^{-2}+x\,R_{A'}+(1-x)\,R_A}+\frac{\sqrt{2}R_O^{-2}}{R_O^{-2}+R_B}\right) \quad (4)$$

where R_A, $R_{A'}$, R_B, and $R_O{}^{2-}$ are the ionic radii of A [Ni^{2+} (0.69 Å)], A′ [Co^{2+} (0.72 Å)], B [Ti^{4+} (0.60 Å)], and [O^{2-} (1.4 Å)], respectively.[31] For the stabilized ilmenite structure 1 > t > 0.745,

Table 1. The obtained lattice parameters and tolerance factor of $NiTiO_3$ and Co-doped $NiTiO_3$ samples.

Samples	Lattice Parameter (Å)		Unit Cell Volume $(Å)^3$	R_{wp}	χ^2	Tolerance Factor (t)
	a = b	c				
NCTO-0	5.0311	13.7981	302.45	9.36	2.41	0.9556
NCTO-5	5.0315	13.7992	302.50	9.89	2.45	0.9553
NCTO-10	5.0348	13.8074	303.10	9.87	2.17	0.9551
NCTO-15	5.0360	13.8131	303.37	9.45	2.87	0.9548
NCTO-17.5	5.0370	13.8176	303.59	10.76	2.92	0.9546
NCTO-20	5.0376	13.8190	303.69	10.89	3.01	0.9545
NCTO-25	5.0408	13.8218	304.36	12.45	3.13	0.9542

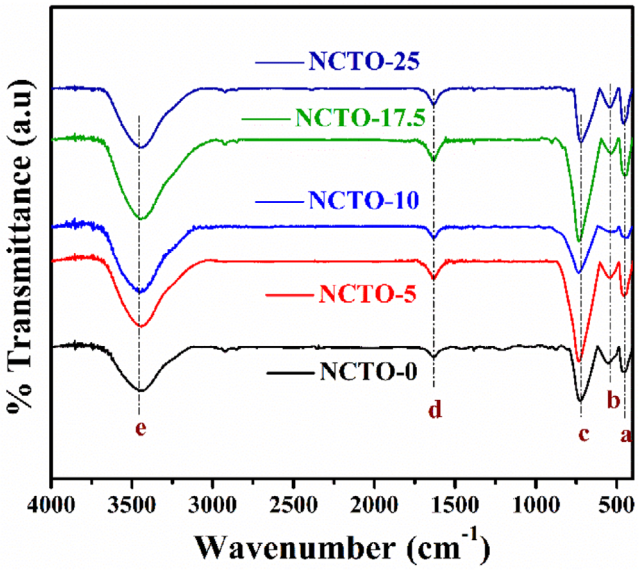

Figure 2. FTIR spectra of NCTO-(0, 5, 10, 17.5, 25) samples.

according to the above Equation 4, substituting Ni^{2+} with larger Co^{2+} ions would slightly decrease the tolerance factor as x increases, but it is still within the range of $1 > t > 0.745$ (Table 1). The tolerance factor (t) for $Ni_{1-x}Co_xTiO_3$ ($x = 0.05, 0.1, 0.15, 0.175, 0.2$, and 0.25), respectively, are 0.9556, 0.9553, 0.9551, 0.9548, 0.9546, 0.9545, and 0.9542.

3.2. FT-IR Analysis

The bonding interactions in the synthesized NCTO powder samples were investigated by recording FT-IR spectra in the region 400–4000 cm^{-1}. The bands in the FT-IR spectra are marked as a, b, c, d, and e. The characteristic vibrational bands of metal-oxygen bonds are observed in the range of 400–700 cm^{-1} in the FT-IR spectrum of NCTO samples, as shown in Figure 2. The strong bands (b) and (c) that appeared at 547 and 717 cm^{-1}, respectively, are mainly due to the stretching vibration modes of Ni—O and Ti—O bonds. The sharp absorption band (a) at 449 cm^{-1} confirms the formation of Ni—O—Ti bonds. The weak absorption band (e) at 3440 cm^{-1} corresponds to the stretching vibration mode of hydroxyl (—OH) groups. The other vibrational bands (d) observed at 1640 cm^{-1} are mainly due to the bending modes of Ti—OH bonds.[32–34] Co doping in $NiTiO_3$ does not significantly alter the stretching frequencies of Ni—O and Ti—O bonds in FTIR spectra (Figure 2), as there is very minute change in the reduced mass of the $Ni_{1-x}Co_xTiO_3$.

3.3. XPS Studies

XPS experiments were carried out to confirm the valence state of the elements (Ni, Ti, and Co) in NCTO-0 and NCTO-17.5 samples. The XPS spectrum Figure 3a,b was deconvoluted using the Voigt peak function and the linear background with the XPS Peak 41 program to precisely determine the double peak characteristics of Ni ($2p_{1/2}$) and Ni ($2p_{3/2}$). The Ni 2p signals at 855.4 and 873.2 eV are attributed to $2p_{3/2}$ and $2p_{1/2}$ of Ni^{2+}, and the additional peaks located at around 861.0 and 879.3 eV are matched to their respective satellite peaks.[35,36] Further, the Ni $2p_{3/2}$ peak was found to be shifted by around 0.2 eV from 855.4 to 855.6 eV in the NCTO-17.5 sample compared to the NCTO-0 sample (no Co-doped sample). This shift confirms the doping of more electronegative ions into the lattice, there is the presence of a certain proportion of Co^{3+} in addition to Co^{2+}, where the more electronegative Co^{3+} ions incorporated into the lattice increase the ionicity of the Ni—O bond through the inductive effect. The deconvoluted Co 2p spectra of NCTO-17.5 (shown in Figure 3c) have $2p_{3/2}$ and $2p_{1/2}$ peaks marked at 781.2 and 796.6 eV, respectively, which belong to Co^{2+} ions (red line), and peaks at 779.8 and 795.4 eV, respectively, belong to Co^{3+} ions (blue line). In addition, there are two satellite peaks at 785.8 and 802.1 eV , indicating that the Co in the NCTO-17.5 is essentially in a + 2 oxidation state.[37] The observed fractional composition of Co^{2+}: Co^{3+} in NCTO-17.5 was 0.88:0.12. The Ti 2p core-level spectra of NCTO-0 and NCTO-17.5 (in Figure 3d,e, respectively), exhibit two peaks centered at 464.1 and 458.5 eV, confirming that Ti is present in the +4 oxidation state.[38,39]

The O 1s spectrum of NCTO-0 and NCTO-17.5 (Figure 3f,g), respectively, was deconvoluted into two peaks at 529.5 and 531.1 eV corresponding to lattice oxygen and surface hydroxyl oxygen, respectively.[2]

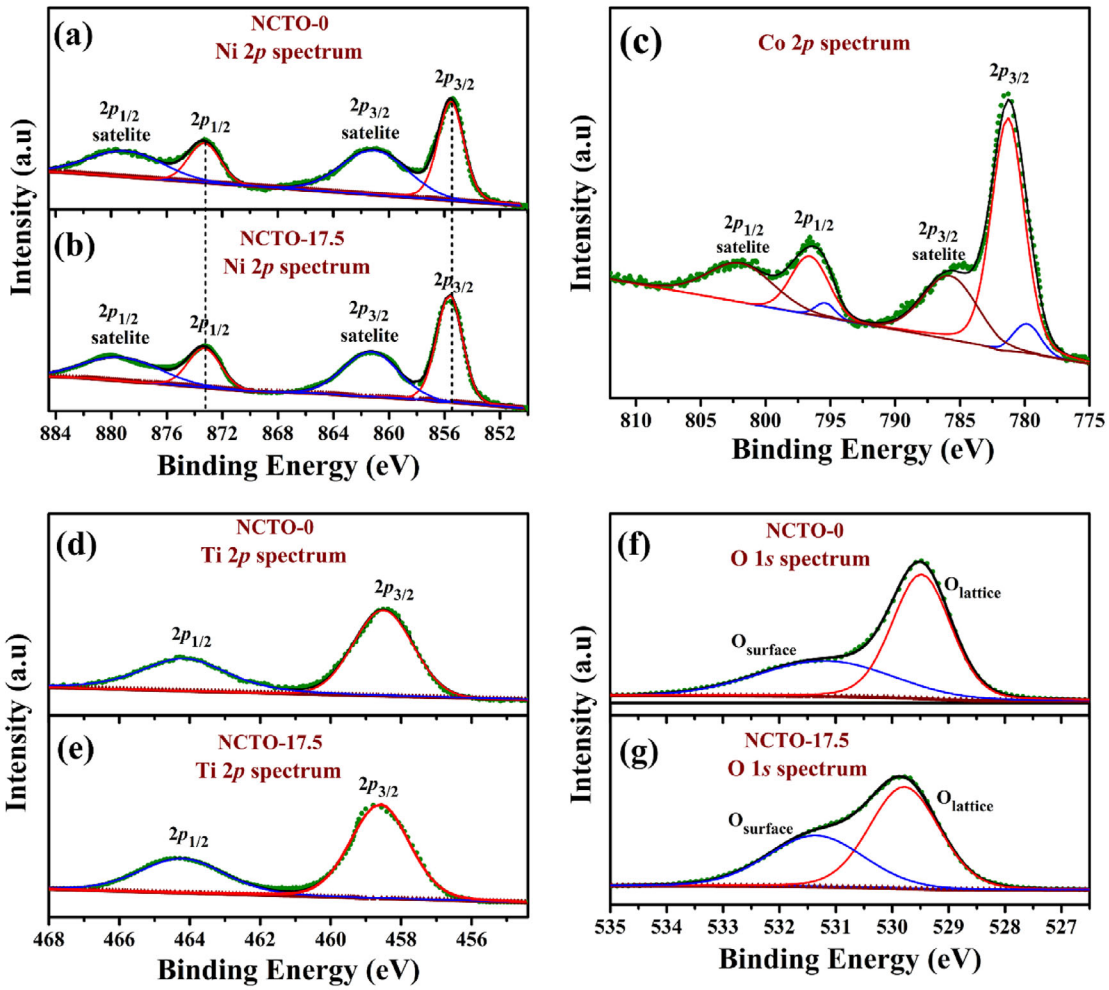

Figure 3. Core level XPS spectrum of (a,b) Ni (2p), (c) Co (2p) (blue and red line colors correspond to the Co^{3+} and Co^{2+} chemical states, respectively), and (d,e) Ti (2p) (f), (g) O (1s).

3.4. Microstructural Analysis

The surface morphology and particle size distribution of the as-synthesized NCTO-0 and NCTO-17.5 samples were studied from the scanning electron micrographs. The SEM image of the NCTO-0 and NCTO-17.5 samples, shown in Figure 4a,b, illustrates the uniform and homogeneous agglomerated particles distributed in the entire region of the micrograph.

The elemental color mapping of the NCTO-0 and NCTO-17.5 samples is shown in the bottom panels of Figure 4a,b, respectively, confirming the homogeneous distribution of the elements in the samples. The microstructure of the synthesized NCTO-17.5 was further confirmed with the bright-field TEM image of the sample (Figure 5a,b), indicating highly crystalline quasi-hexagonal particles existing in the synthesized material. The polyhedral shape of the particle was further confirmed through TEM analysis. The length of the faces and the diameter of the polyhedral-shaped particle are measured using ImageJ software and given in Figure 5b.

It shows that the length of the side faces is approximately in the range of 50–60 nm, and the diameter of the particle is approximately 112 nm. The lattice fringes of the NCTO-17.5 samples, in Figure 5c, correspond to the (110) plane and are in accordance with the XRD studies of the powder samples. The interplanar distances measured from the selected area electron diffraction (SAED) pattern show good agreement with the rhombohedral $NiTiO_3$. The diffraction rings are indexed to (012), (104), (110), and (11–3) from the inside to the outside and match well with the XRD results.

3.5. Electrochemical Studies

3.5.1. OER Performances of Synthesized Catalysts

The electrochemical performance of $Ni_{1-x}Co_xTiO_3$ ($0 \leq x \leq 0.25$) catalysts toward the OER was investigated in O_2-saturated 1 M KOH at a scan rate of 5 mVs^{-1} using a three-electrode setup. Before collecting the data in the range of 1.2 to 1.8 V versus RHE, several cycles of fast-scan CV were conducted on the working electrode to achieve a stable current before collecting the data. The effect of different concentration of KOH electrolyte with pH ranging from 13 to 14.3 was tested and best activity was observed for 1 M KOH, hence all the catalysts testing were performed in

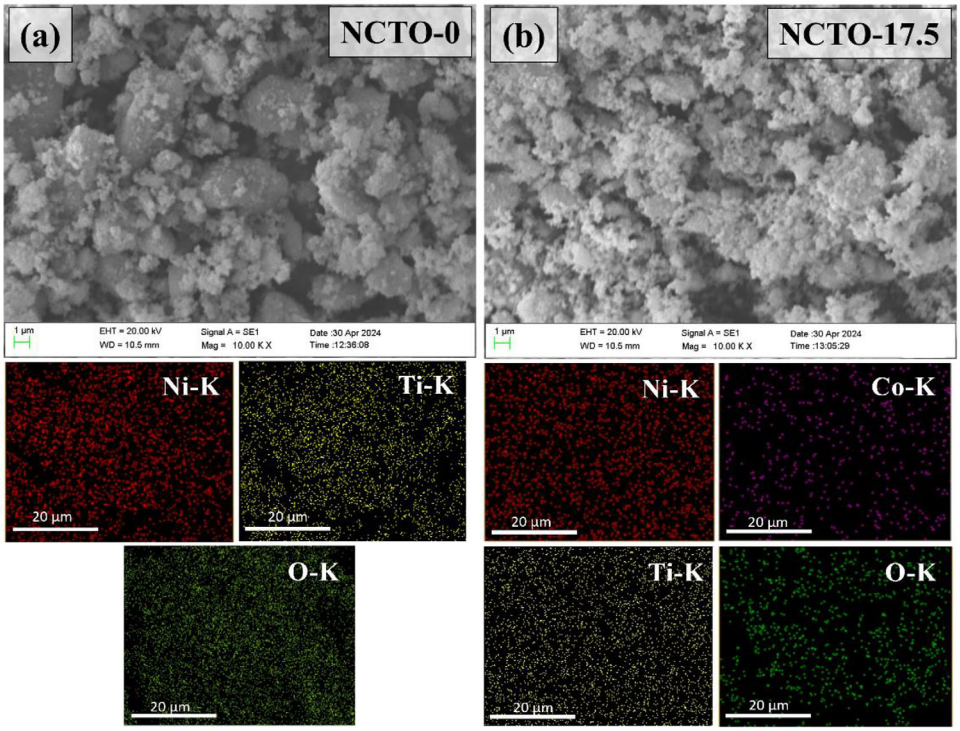

Figure 4. SEM micrograph of (a) NCTO-0 (the scale bars are 1 µm), bottom two left panels represent elemental mapping of individual elements (Ni, Ti, and O) present in the NCTO-0 and (b) NCTO-17.5 (the scale bars are 1 µm), bottom two right panels represent elemental mapping of individual elements (Ni, Co, Ti, and O) present in the NCTO-17.5 sample.

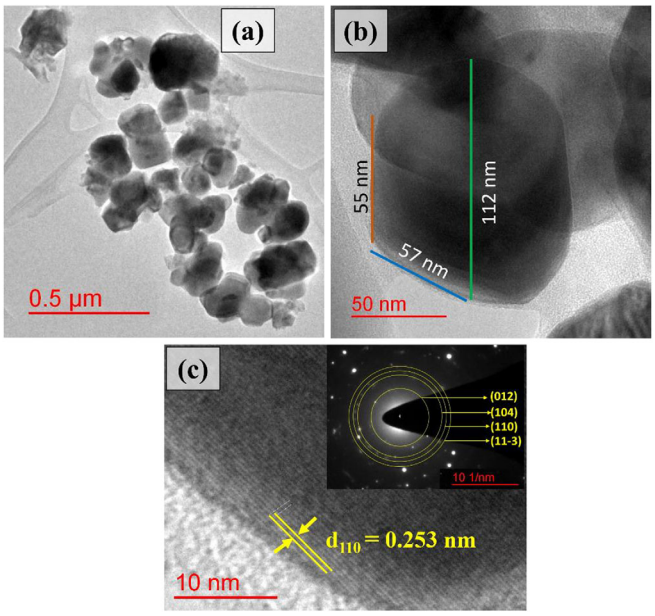

Figure 5. Bright-field TEM images (a,b) NCTO-17.5, and (c) HR-TEM image with interplanar *d*-spacing of (110) plane for NCTO-17.5; inset shows the SAED pattern.

the same concentration. The effect of different concentration of KOH electrolytes on OER activity of NCTO-17.5 is given in Figure S1, Supporting Information.

The LSV curves, in Figure 6a, show the OER performances of all the synthesized NCTO catalysts following the order NCTO-0 < NCTO-5 < NCTO-10 < NCTO-25 < NCTO-20 < NCTO-15 < NCTO-17.5. OER activity reaches its optimum performance for 17.5% Co doping and the activity decreases with further increase in the dopant concentration. Based on 10% solar water splitting conversion efficiency, the overpotential (η) needed to achieve a current density of 10 mA cm^{-2} is an important parameter in solar fuel synthesis. Consequently, it is important to compare the overpotential of the catalyst samples at this current density.[6] The overpotential in this context is defined as the difference between the observed OER potential at 10 mA cm^{-2} and the theoretical reversible potential (1.23 V versus RHE). The overpotential needed to achieve a current density of 10 mA cm^{-2} for NCTO-*s* (s = 0 to 25% doping) was determined to be 510, 482, 464, 416, 395, 428, and 445 mV, respectively, as depicted in Figure 6b.

Tafel analysis stands as a fundamental study in the assessment of electrocatalysts for water electrolysis. The Tafel slope, illustrating the correlation between potential and the logarithm of current density, holds significance in evaluating reaction kinetics.[40]

Figure 6c shows the Tafel plot of a series of $Ni_{1-x}Co_xTiO_3$ ($0 \leq x \leq 0.25$) samples and the Tafel slope values obtained for NCTO-0, NCTO-5, NCTO-10, NCTO-15, NCTO-17.5, NCTO-20, and NCTO-25 are approximately 118, 101, 92, 65, 56, 72, and 84 mV dec^{-1}, respectively. A low Tafel slope value signifies a superior electrocatalyst with reduced overpotential. The lowest Tafel value observed for NCTO-17.5 (56 mV dec^{-1}) suggests its faster reaction kinetics compared to all other Co-doped $NiTiO_3$ catalysts. EIS measurements were performed to obtain

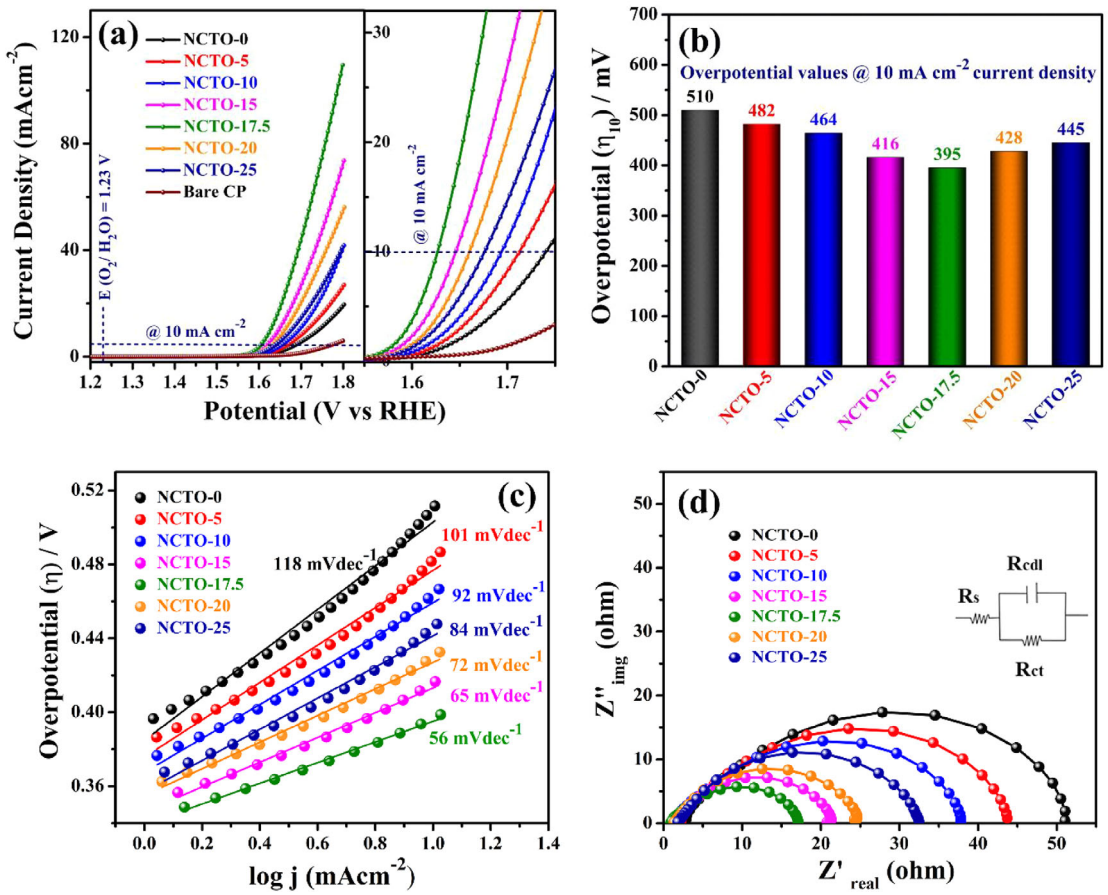

Figure 6. OER performance of NCTO series samples $Ni_{1-x}Co_xTiO_3$ (x = 0.05, 0.1, 0.15, 0.175, 0.2, 0.25). (a) Linear sweep voltammograms taken at a scan rate of 5 mV s^{-1} in 1 M KOH, (b) overpotentials at a current density of 10 mA cm^{-2}, (c) Tafel plots, (d) EIS recorded at 1.6 V versus RHE.

the impedance spectra and analyzed for determining the R_{ct}, among other parameters, providing insights into the electrochemical performance and efficiency of the catalysts under investigation. Impedance studies for the catalysts $Ni_{1-x}Co_xTiO_3$ were conducted in the frequency range of 10–100 kHz with an AC amplitude of 10 mV at a potential of 1.6 V versus RHE, as shown in Figure 6d. Additionally, an equivalent circuit fit of the EIS data in the inset of Figure 6d, shows the solution resistance (R_s), charge-transfer resistance (R_{ct}), and double-layer capacitance (R_{Cdl}). The charge transfer resistance (R_{ct}) (diameter of the semicircle in the Nyquist plot at the high-frequency region) is linked with the electrochemical kinetics of the reaction. A smaller semicircle loop suggests lower charge-transfer resistance and a sign of faster kinetics during the OER process.[41,42] The R_{ct} value of NCTO-17.5 is found to be 16.13 Ω, which is lower than all other synthesized catalysts NCTO-0 (48.24 Ω), NCTO-5 (41.31 Ω), NCTO-10 (36.10 Ω), NCTO-15 (19.70 Ω), NCTO-20 (23.11 Ω), and NCTO-25 (30.31 Ω), indicating its faster OER kinetic rate compared to the other catalysts.

Moreover, the electrochemically active surface area (ECSA) of each catalyst was determined using double-layer capacitance measurement to investigate the intrinsic characteristics of the electrocatalyst. The double-layer capacitance (C_{dl}) is evaluated using CV in a non-Faradaic potential range of 0.91 to 1.01 V. The scan rates used in the analysis vary from 40 to 140 mV/s, as depicted in Figure 7a–g. The change in current density (ΔJ) during anodic and cathodic sweeps in CV is influenced by the charge-storage capacity of the working electrode and shows a linear increase as the scan rate increases.[42,43]

The double-layer capacitance which is the slope of $\Delta J/2$ versus scan rate plot is found to be 0.36, 0.41, 0.53, 0.70, 0.76, 0.66, and 0.61 mF/cm^{-2} for all the NCTO series catalysts, which follows the order NCTO-0 < NCTO-5 < NCTO-10 < NCTO-25 < NCTO-20 < NCTO-15 < NCTO-17.5 as plotted (Figure 8a) for each catalyst. The best electrocatalytic OER activity was obtained for NTO-17.5 or up to 17.5% Co doping in $NiTiO_3$, and OER activity decreases with further increase in Co doping at the Ni site in $NiTiO_3$ ilmenite structure.

The electrochemical active surface area (ECSA) of a catalyst is calculated using the double-layer capacitance with the formula:

$$ECSA = C_{dl}/C_s \quad (5)$$

In this equation, C_{dl} represents the double-layer capacitance of the catalyst, while C_s denotes the specific capacitance of the material per unit area under identical electrolyte conditions, which is established as 0.04 mF cm^{-2} in a 1.0 M KOH solution.[44] The relationship between ECSA and the catalyst is depicted in Figure 8b, where it is evident that ECSA is highest for NCTO-17.5,

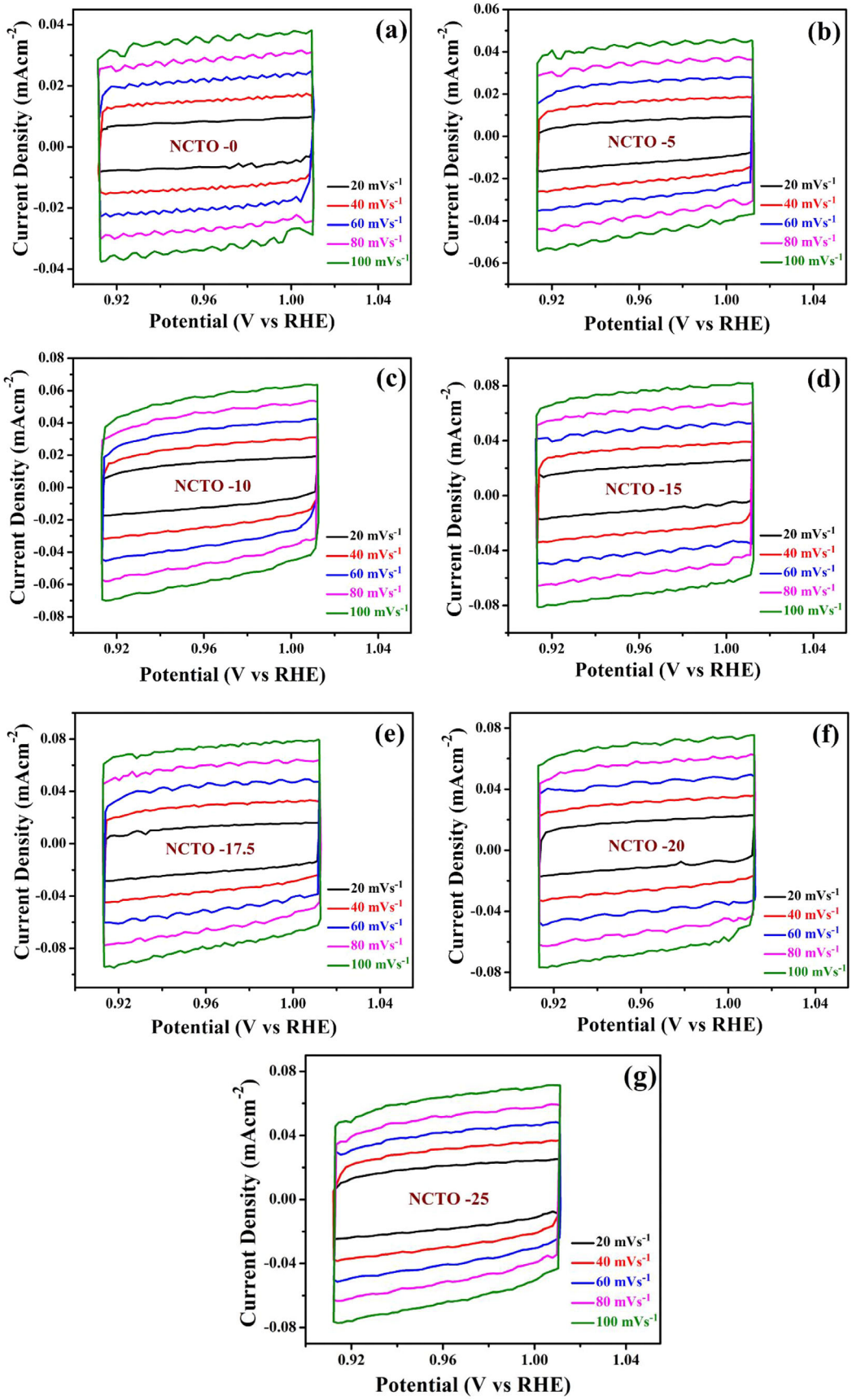

Figure 7. Determination of double layer capacitance (C_{dl}) of NCTOs (a–g) CV measurements in a non-Faradaic current region (0.9–1.0 V versus RHE) at scan rates of 20, 40, 60, 80, and 100 mV s^{-1} in 1 M KOH electrolyte.

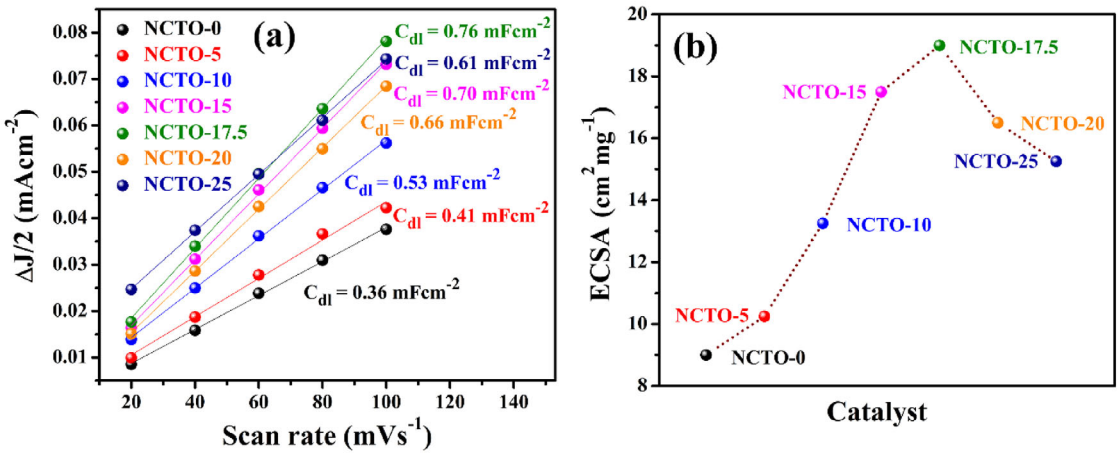

Figure 8. (a) Plots of capacitive current density differences $\Delta J/2$ versus the scan rate for all NCTO samples and (b) plot of ECSA versus catalyst $Ni_{1-x}Co_xTiO_3$ (x = 0.05–0.25).

Table 2. The C_{dl} and corresponding ECSA values of all the catalysts.

S. No.	Catalyst	C_{dl} (mF cm^{-2})	ECSA (cm^2 mg^{-1})
1	NCTO-0	0.36	9
2	NCTO-5	0.41	10.25
3	NCTO-10	0.53	13.25
4	NCTO-15	0.70	17.5
5	NCTO-17.5	0.76	19
6	NCTO-20	0.66	16.5
7	NCTO-25	0.61	15.25

after which no further increase in ECSA is observed. The values of C_{dl} and the corresponding ECSA for all catalysts examined in this study are detailed in Table 2.

3.5.2. Long-Term Stability Test

The stability of electrocatalysts is a critical factor for large-scale water electrolysis applications.[45] The static stability of NCTO-17.5 was evaluated through a chronoamperometric (CA) test conducted at 1.62 V versus RHE for 60 h, as shown in Figure 9. The results demonstrate that NCTO-17.5 exhibits a stable current density at a fixed applied potential with a current retention of ~94% at 1.62 V operating voltage versus RHE. The stability of the NCTO-17.5 catalyst was evaluated through an accelerated degradation test (ADT) using fast-scan CV cycling in a potentiodynamic mode. The stability of this catalyst over several CV cycles makes the electrocatalytic mechanism of $NiTiO_3$ very different in comparison to those based on dissolution/redeposition recently demonstrated for the Ni/Fe-based counterparts.[46,47]

The test involved scanning 1000 CV cycles at a scan rate of 100 mV/s within a potential range of 1.2–1.8 V versus RHE. The inset of Figure 9 shows the LSV plots for the 1st, 100th, 500th, and 1000th cycles. The results indicate only a marginal change in the overpotential at 10 mA cm^{-2} throughout the 1000 cycles. This suggests that the NCTO-17.5 catalyst exhibits excellent stability under the highly alkaline conditions of the 1 M KOH electrolyte.

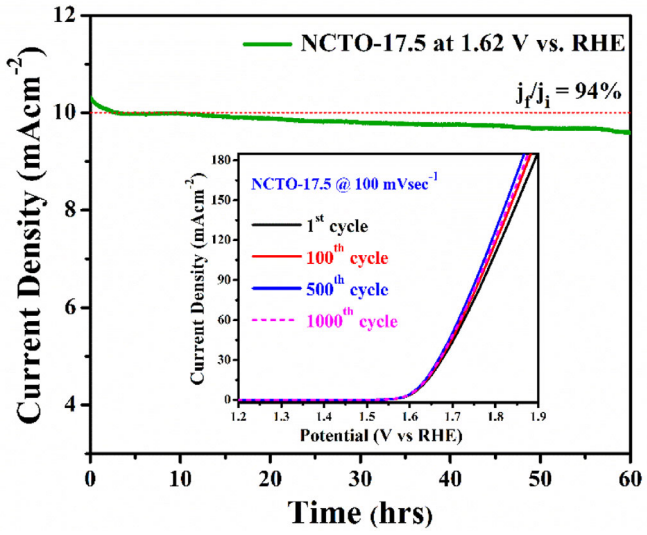

Figure 9. Chronoamperogram of NCTO-17.5 at an applied potential of 1.62 V versus RHE for 24 h; inset shows the linear sweep voltammograms for the 1st, 100th, 500th, and 1000th cycle at a scan rate of 100 mV s^{-1}.

3.5.3. Post OER Characterization

The stability of the electrocatalyst NCTO-17.5 after extended electrochemical cycling was further verified through a post-characterization technique, that is, post X-ray diffraction (XRD). The XRD analysis conducted on the NCTO-17.5 electrode after electrochemical testing revealed no changes in the diffraction pattern, except for a peak attributed to the carbon paper substrate. This indicates that the structural retention of the NCTO-17.5 catalyst is maintained after long-term electrochemical testing. The diffraction pattern aligns with the rhombohedral phase R-3 (148) $NiTiO_3$, indexed well using the (JCPDS no. 33–0960), as illustrated in Figure 10.

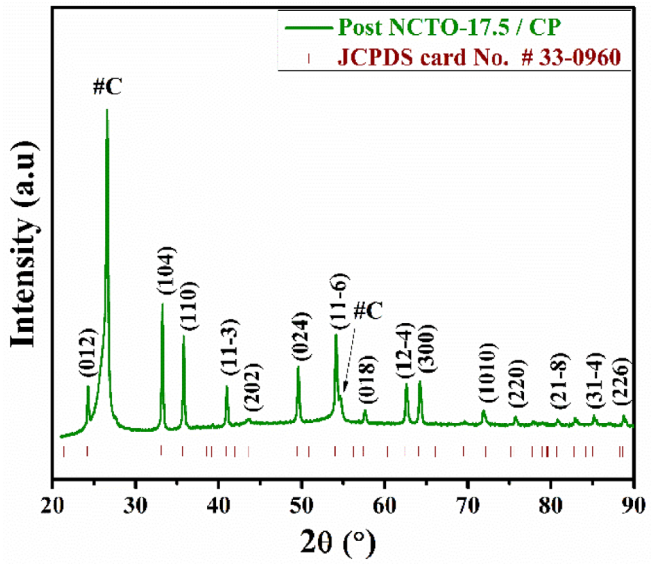

Figure 10. Post-OER XRD pattern of NCTO-17.5 electrode.

4. Conclusion

In summary, a series of ilmenite type Co-doped $NiTiO_3$ ($Ni_{1-x}Co_xTiO_3$, $0 < x < 0.25$) have been synthesized by the sol–gel route and investigated for the influence of Co doping on electrocatalytic activity toward the oxygen evolution reaction. 17.5% Co-doped $NiTiO_3$ is found to be the best OER catalyst in the series of $Ni_{1-x}Co_xTiO_3$($0 < x < 0.25$). The observed higher activity of Co-doped $NiTiO_3$ is due to the inductive effect generated by Co substitution at the Ni site in the ilmenite structured $NiTiO_3$. $Ni^{2+/3+}$ is the active site for OER as Ni(3d) orbital are pinned over O(2p) orbitals. Synergistic interaction between Ni and Co generates the inductive effect resulting from the difference in the electronegativity of Co and Ni which enhances the ionicity of Ni—O bond leading to superior OER activity of the catalyst. XPS study confirms the high electro-positivity of Ni ions. The higher ionicity of Ni—O leads to a greater overlap between Ni(3d) and O(2p) orbital resulting in a higher catalytic activity of the doped catalysts. An increase in the Co concentration beyond an optimum level leads to a decrease in the OER activity of the catalyst as with a higher substitution of Co on the Ni site, the concentration of catalytic active centers ($Ni^{2+/3+}$) decreases in the catalyst. An optimum concentration of 17.5% Co doping leads to the best activity via its inductive effect on the redox potential of the active species, namely Ni^{2+}/Ni^{3+} parent species. Also, this optimum concentration of 17.5% Co in $NiTiO_3$ shows the best OER activity and $Ni_{0.825}Co_{0.175}TiO_3$ depicts a Tafel slope of 56 mV dec^{-1} and an overpotential of 395 mV at a current density of 10 mA cm^{-2}. This opens up an approach for altering the catalytic activity by testing the inductive effect of the different dopant ions on the parent catalyst.

Acknowledgements

Dr. Asha Gupta gratefully acknowledges the Science and Engineering Research Board (SERB), India, for financial support through Start-Up Research Grant SRG Project no. SRG/2019/000605 (Chy/19–20/03). The authors also thank the Department of Chemistry, IIT (BHU), for its facility and support, and gratefully acknowledge the use of characterization facilities and services at CIFC, IIT (BHU), Varanasi.

Conflict of Interests

The authors declare no conflict of interest.

Data Availability Statement

The data that support the findings of this study are available in the supplementary material of this article.

Keywords: Co doped $NiTiO_3$ · Electrocatalysis · Ilmenite structure · Inductive effect · Oxygen evolution reaction

[1] J. A. Turner, *Science* **2004**, *305*, 972–974.
[2] A. Gupta, V. Kushwaha, R. Mondal, A. N. Singh, R. Prakash, K. D. Mandal, P. Singh, *Phys. Chem. Chem. Phys.* **2022**, *24*, 11066–11078.
[3] S. Kumar, R. Ranjeeth, N. K. Mishra, R. Prakash, P. Singh, *Dalton Trans.* **2022**, *51*, 5834–5840.
[4] V. Soni, A. N. Singh, P. Singh, A. Gupta, *RSC Adv.* **2022**, *12*, 18794.
[5] V. Soni, S. Jaiswal, K. G. Nigam, P. Singh, A. Gupta, *J. Mater. Chem. A Mater.* **2024**, *12*, 19212–19226.
[6] V. Soni, S. Jaiswal, P. Singh, A. Gupta, *ACS Appl. Energy Mater.* **2024**, *7*, 3175–3186.
[7] R. Mondal, H. Ratnawat, S. Mukherjee, A. Gupta, P. Singh, *Energy Fuels* **2022**, *36*, 3219.
[8] N. Han, W. Zhang, W. Guo, H. Pan, B. Jiang, L. Xing, H. Tian, G. Wang, X. Zhang, J. Fransaer, *Nanomicro Lett.* **2023**, *15*, 185.
[9] T. Thippani, S. Mandal, G. Wang, V. K. Ramani, R. Kothandaraman, *RSC Adv.* **2016**, *6*, 71122.
[10] D. Liu, Z. Zhao, Z. Xu, L. Li, S. Lin, *Dalton Trans.* **2022**, *51*, 12839–12847.
[11] M. Gong, H. Dai, *Nano Res.* **2015**, *8*, 23–39.
[12] W. Moschkowitsch, K. Dhaka, S. Gonen, R. Attias, Y. Tsur, M. Caspary Toroker, L. Elbaz, *ACS Catal.* **2020**, *10*, 4879–4887.
[13] R. Mondal, H. Ratnawat, S. Kumar, A. Kumar, P. Singh, *RSC Adv.* **2020**, *10*, 17845.
[14] J. A. Brehm, J. W. Bennett, M. R. Schoenberg, I. Grinberg, A. M. Rappe, *J. Chem. Phys.* **2014**, *140*, 224703.
[15] S. Lettieri, M. Pavone, A. Fioravanti, L. Santamaria Amato, P. Maddalena, *Materials* **2021**, *14*, 1645.
[16] J. O. Bockris, T. Otagawa, *J. Electrochem. Soc.* **1984**, *131*, 290–302.
[17] N. T. Suen, S. F. Hung, Q. Quan, N. Zhang, Y. J. Xu, H. M. Chen, *Chem. Soc. Rev.* **2017**, *46*, 337–365.
[18] T. N. Lambert, J. A. Vigil, S. E. White, D. J. Davis, S. J. Limmer, P. D. Burton, E. N. Coker, T. E. Beechem, M. T. Brumbach, *Chem. Commun.* **2015**, *51*, 9511–9514.
[19] G. Wu, N. Li, D.-R. Zhou, K. Mitsuo, B.-Q. Xu, *J. Solid State Chem.* **2004**, *177*, 3682–3692.
[20] X. Yan, K. Li, L. Lyu, F. Song, J. He, D. Niu, L. Liu, X. Hu, X. Chen, *ACS Appl. Mater. Interfaces* **2016**, *8*, 3208–3214.
[21] Y. Zhao, X. Jia, G. Chen, L. Shang, G. I. N. Waterhouse, L.-Z. Wu, C.-H. Tung, D. O'Hare, T. Zhang, *J. Am. Chem. Soc.* **2016**, *138*, 6517–6524.
[22] Y. Yang, L.-C. Kao, Y. Liu, K. Sun, H. Yu, J. Guo, S. Y. H. Liou, M. R. Hoffmann, *ACS Catal.* **2018**, *8*, 4278–4287.
[23] B. S. Kumar, K. Tarafder, A. R. Shetty, A. C. Hegde, V. C. Gudla, R. Ambat, S. K. Kalpathy, S. Anandhan, *Dalton Trans.* **2019**, *48*, 12684–12698.
[24] C. Dong, X. Liu, X. Wang, X. Yuan, Z. Xu, W. Dong, M. S. Riaz, G. Li, F. Huang, *J. Mater Chem. A Mater.* **2017**, *5*, 24767–24774.
[25] D. A. Kuznetsov, B. Han, Y. Yu, R. R. Rao, J. Hwang, Y. Román-Leshkov, Y. Shao-Horn, *Joule* **2018**, *2*, 225–244.
[26] H. Chen, W. Fu, Z. Geng, J. Zeng, B. Yang, *J. Mater. Chem. A Mater.* **2021**, *9*, 4626–4647.

[27] W. Jiang, W. Lehnert, M. Shviro, *ChemElectroChem* **2023**, *10*, e202200991.
[28] V. Kushwaha, A. Gupta, R. B. Choudhary, K. D. Mandal, R. Mondal, P. Singh, *Phys. Chem. Chem. Phys.* **2023**, *25*, 555–569.
[29] R. Tursun, Y. C. Su, Q. S. Yu, J. Tan, T. Hu, Z. B. Luo, J. Zhang, *J. Alloys Compd.* **2019**, *773*, 288–298.
[30] X. Liu, R. Hong, C. Tian, *J. Mater. Sci.: Mater. Electron.* **2009**, *20*, 323.
[31] R. D. Shannon, C. T. Prewitt, *Acta Crystallogr. B* **1969**, *25*, 925–946.
[32] C. Pavithra, W. Madhuri, *Mater. Chem. Phys.* **2018**, *211*, 144–149.
[33] S. Gaddimath, K. B. Chandrakala, A. Lagashetty, S. Dani, C. P. Prabhu, K. Giddaerappa, L. K. Sannegowda, *J. Appl. Electrochem.* **2024**, *54*, 2519–2536.
[34] A. P. Souri, N. Andrigiannaki, M. Moschogiannaki, V. Faka, G. Kiriakidis, A. Malankowska, A. Zaleska-Medynska, V. Binas, *Appl. Sci.* **2021**, *11*, 10850.
[35] T. Lakshmi, N. Hajarabeevi, T. Mishra, N. Aman, *Optik* **2024**, *298*, 171561.
[36] S. Sahoo, A. K. Satpati, P. K. Sahoo, P. D. Naik, *ACS Omega* **2018**, *3*, 17936–17946.
[37] J. Huang, W. Qian, H. Ma, H. Zhang, W. Ying, *RSC Adv.* **2017**, *7*, 33441.
[38] S. Jaiswal, R. Mondal, V. Kushwaha, A. Gupta, P. Singh, *ACS Appl. Energy Mater.* **2023**, *6*, 7323–7334.
[39] W. Xie, R. Li, Q. Xu, *Sci. Rep.* **2018**, *8*, 8752.
[40] T. Shinagawa, A. T. Garcia-Esparza, K. Takanabe, *Sci. Rep.* **2015**, *5*, 13801.
[41] V. Soni, R. Mondal, A. N. Singh, P. Singh, A. Gupta, *ACS Appl. Energy Mater.* **2023**, *6*, 1308–1320.
[42] X. Liu, Z. Y. Zhai, Z. Chen, L. Z. Zhang, X. F. Zhao, F. Z. Si, J. H. Li, *Catalysts* **2018**, *8*, 310.
[43] S. Jaiswal, V. Soni, P. Singh, A. Gupta, *ACS Appl. Energy Mater.* **2024**, *7*, 8814–8825.
[44] C. C. L. McCrory, S. Jung, J. C. Peters, T. F. Jaramillo, *J. Am. Chem. Soc.* **2013**, *135*, 16977–16987.
[45] S. Anantharaj, S. R. Ede, K. Sakthikumar, K. Karthick, S. Mishra, S. Kundu, *ACS Catal.* **2016**, *6*, 8069–8097.
[46] L. Ciambriello, I. Alessandri, L. Gavioli, I. Vassalini, *ChemCatChem* **2024**, *16*, e202400286.
[47] L. Ciambriello, I. Alessandri, M. Ferroni, L. Gavioli, I. Vassalini, *ACS Appl. Energy Mater.* **2024**, *7*, 3462–3472.

Manuscript received: March 6, 2025
Revised manuscript received: April 15, 2025
Accepted manuscript online: April 16, 2025
Version of record online: May 13, 2025